

# Time-reversal symmetry breaking Weyl semimetal and tunable quantum anomalous Hall effect in a two-dimensional metal-organic framework

Xiaoming Zhang,<sup>1</sup> Yefeng Li,<sup>1</sup> Tingli He<sup>✉</sup>,<sup>1</sup> Min Zhao,<sup>1</sup> Lei Jin,<sup>1</sup> Cong Liu,<sup>1</sup> Xuefang Dai,<sup>1</sup> Ying Liu,<sup>1,\*</sup> Hongkuan Yuan<sup>✉</sup>,<sup>2,†</sup> and Guodong Liu<sup>1,‡</sup>

<sup>1</sup>State Key Laboratory of Reliability and Intelligence of Electrical Equipment, and School of Materials Science and Engineering, Hebei University of Technology, Tianjin 300130, China

<sup>2</sup>School of Physical Science and Technology, Southwest University, Chongqing, China



(Received 11 April 2023; accepted 24 July 2023; published 4 August 2023)

Exploring the relationship between magnetism and band topology has become a popular research topic in condensed matter physics. In this work, we investigate this interplay in a two-dimensional (2D) metal-organic framework (MOF)  $\text{Mn}_3(\text{C}_6\text{O}_6)_2$ . We discover that this MOF has a “soft” ferromagnetic property, making it possible to control the topological phases by adjusting the magnetization direction. In its ground state, the MOF has Weyl points precisely located at the Fermi level and only in one spin channel, which means it can be described as an ideal, fully spin-polarized 2D Weyl semimetal. We determine that the stability of these Weyl points is protected by the vertical mirror symmetries. Particularly, the Weyl point can be preserved even with considering the spin-orbital coupling, with an in-plane magnetization direction parallel to the mirror normal vector. By altering the in-plane magnetization away from the normal vector of the vertical mirror symmetry, we demonstrate that the Weyl point is gapped, transformed into the quantum anomalous Hall (QAH) phase, resulting in a chiral edge state at the boundary. We calculate a Chern number to capture the main feature of the QAH, which indicates quantized Hall conductance. Furthermore, by rotating the magnetization direction in the plane, we discover that the Weyl point is a critical point where the QAH changes the sign of the Chern number, along with inverting the propagating direction of the chiral edge state. Overall, our findings highlight  $\text{Mn}_3(\text{C}_6\text{O}_6)_2$  as a promising material candidate for studying the interplay between topology and magnetism, Weyl semimetal, and QAH phases.

DOI: [10.1103/PhysRevB.108.054404](https://doi.org/10.1103/PhysRevB.108.054404)

## I. INTRODUCTION

Weyl semimetals (WSMs) are currently attracting significant interest in condensed matter physics [1–6]. In a WSM, the conduction and valence bands cross linearly at isolated double degenerate Weyl points, where the electrons behave like relativistic Weyl fermions. Weyl points appear in pairs, characterized by Chern number  $\pm 1$  according to the no-go theorem [7]. On the surfaces of WSMs, the constant energy surface encloses one of the Weyl points of the pair with opposite Chern number, forming a Fermi arc [8]. The topological properties of WSMs lead to extraordinary characteristics such as ultrahigh mobility [2,9], negative magnetoresistance [10–14], colossal photovoltaic response [15], and excellent catalytic performance [16–20].

In a three-dimensional (3D) WSM, an electron near the Weyl point could be effectively described as ( $\hbar = 1$ ),

$$\mathcal{H}_{\text{WSM}}^{3D}(k) = vk\sigma, \quad (1)$$

$v$  denotes the Fermi velocity, and  $\sigma$  is the Pauli matrix corresponding to real or pseudospin. Based on its effective model,

one could infer that any small perturbation cannot destroy the Weyl point but only move its position in momentum space [21]. Therefore, a 3D Weyl point does not require additional symmetric protection. However, its existence necessitates the breaking of time-reversal symmetry ( $T$ ) or spatial inversion symmetry ( $P$ ). This is because the combined operation of  $PT$  results in a double degeneracy of each band due to the degeneracy of spin-up and spin-down states when considering spin-orbit coupling (SOC). Consequently, the band crossings of these two bands form a Dirac point (a fourfold band crossing) rather than a Weyl point [22].

In comparison to 3D bulk materials, two-dimensional (2D) systems are much easier to control, making them an attractive avenue for the extension of the concept of WSMs. However, the squeezing of dimensionality in 2D systems requires additional symmetry, such as mirror symmetry or rotation symmetry, to protect the Weyl point [23]. Otherwise, any perturbation with  $\sigma_z$  will gap the Weyl point (say the Weyl point losing its dimensionality in the  $z$  direction). In addition, breaking  $T$  or  $P$  is also necessary for the appearance of a 2D Weyl point. Interestingly, breaking  $T$  is also a prerequisite for the quantum anomalous Hall effect (QAHE) in 2D systems. The QAHE is a gapped topological phase characterized by the quantized Hall conductance with dissipationless chiral edge states pinned at the boundary of the sample [24,25]. Materials that realize the QAHE possess great potential in topological transistors.

\*ying\_liu@hebut.edu.cn

†yhk10@swu.edu.cn

‡gdliu1978@126.com

A general way to break time-reversal symmetry is by introducing magnetic ordering [26–30]. Therefore, a magnetic system may provide a platform to investigate the interplay between magnetism and topology. Moreover, magnetization strongly affects the time and spatial symmetries of the lattice, making it possible to achieve a topological phase transition by tuning the magnetization. In fact, the transition between 2D WSMs and the QAHE has been achieved in monolayer ferromagnetic materials, PtCl<sub>3</sub> [31] and YN<sub>2</sub> [32], by controlling their “soft” magnetic property. However, the search for materials with intrinsic soft magnetic properties is still limited, and there is an urgent need to identify more promising materials.

2D metal-organic frameworks (MOFs) are an important class of 2D materials that consist of metal ions coordinated with organic ligands to form porous crystalline structures. Due to their diverse structures and functions, MOFs have garnered significant interest among researchers [33–35]. In particular, MOFs containing transition metals have been shown to exhibit nontrivial band topologies, such as the topological Weyl half-semimetal (WHS) state and the QAHE [36–38]. In our study, we focus on a ferromagnetic 2D MOF material, Mn<sub>3</sub>(C<sub>6</sub>O<sub>6</sub>)<sub>2</sub>, which we find to be a WHS material with a fully spin-polarized Weyl point located precisely at the Fermi level in the absence of SOC. When SOC is included, the spin-polarized Weyl point can still be preserved with a vertical mirror symmetry permitted by magnetization. If this symmetry is not present, the phase will transform into a QAH phase characterized by a Chern number ( $|C| = 1$ ). Interestingly, Mn<sub>3</sub>(C<sub>6</sub>O<sub>6</sub>)<sub>2</sub> exhibits soft ferromagnetic ground states, and the in-plane magnetization can be easily tuned. This makes it possible to realize the transition between the WHS and QAH phases. Importantly, the Weyl point is a critical point at which the QAH changes its Chern number from  $C = +1$  to  $C = -1$ , while also switching the propagating direction of edge states. Therefore, our findings provide a concrete example for studying the transition between WHS and QAH phases and offer a magnetic material platform for topological spintronics.

## II. COMPUTATIONAL METHODS

We perform the first-principles calculations in the framework of density-functional theory (DFT) within the Vienna *Ab initio* simulation package (VASP) [39,40]. The exchange correlation effect is treated in the conventional local density approximation (LDA) and generalized gradient approximation (GGA) in the Perdew-Burke-Ernzerhof function [41,42]. We also adopted GGA+*U* and LDA+*U* strategies to describe the strong Coulomb interaction between the partially filled 3*d* shells of the transition metals in the materials. A 16-Å-thick vacuum layer is used to ensure decoupling between neighboring slabs. All calculations are performed with a plane-wave cutoff of 500 eV and the convergence criterion for the electronic self-consistency loop was set to be 10<sup>-7</sup> eV on the 11 × 11 × 1 Monkhorst-Pack *k*-point mesh; and for the structural relaxation, the Hellmann-Feynman forces on each atom were taken to be 0.01 eV/Å [43]. The VESTA package was used for the illustration of atomic structures [44]. The topological features of edge states were calculated based on

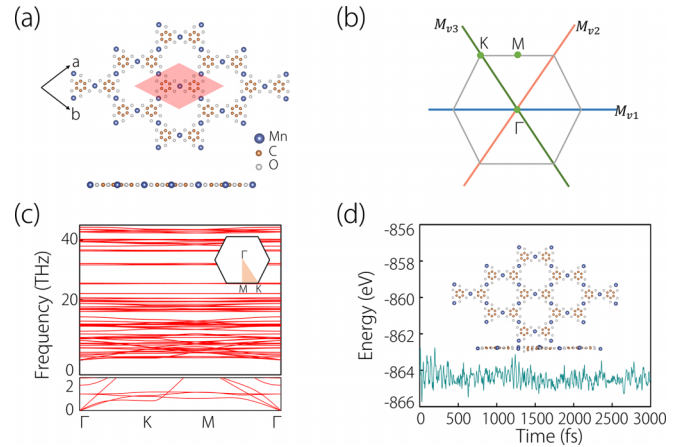


FIG. 1. (a) Top and side views of the monolayer Mn<sub>3</sub>(C<sub>6</sub>O<sub>6</sub>)<sub>2</sub>. (b) We mark the orientation of the three vertical mirror planes for the lattice structure (red, blue, and green lines). (c) Phonon dispersion of Mn<sub>3</sub>(C<sub>6</sub>O<sub>6</sub>)<sub>2</sub>. A 3 × 3 × 1 supercell is used in the calculation. The inset figure indicates the first Brillouin zone with high-symmetry points labeled. (d) *Ab initio* molecular dynamics of Mn<sub>3</sub>(C<sub>6</sub>O<sub>6</sub>)<sub>2</sub> at 300 K.

maximally localized Wannier functions [45,46], realized using the WANNIERTOOLS package [47].

## III. RESULTS AND DISCUSSION

### A. Crystal structure, stability, and magnetic ordering

The lattice structure of the monolayer Mn<sub>3</sub>(C<sub>6</sub>O<sub>6</sub>)<sub>2</sub> is displayed in Fig. 1(a), which shows that it consists of a single layer of atoms all lying in the same plane. The framework is composed of Mn ions that form a kagome lattice, which is linked by organic ligands consisting of C and O atoms. The highlighted region in the figure indicates that the primitive cell of the lattice contains 3 Mn atoms, 12 C atoms, and 12 O atoms. The lattice has a space group of *P6/mmm* (No. 191), which is generated by a threefold rotation symmetry, a vertical mirror symmetry, a horizontal mirror symmetry, and the inversion symmetry *P*. Because of the threefold rotation symmetry, there are three equal vertical mirror symmetries denoted as *M<sub>vi</sub>* ( $i = 1, 2, 3$ ) as shown in Fig. 1(b), and these symmetries play a significant role in the stability of 2D Weyl points that will be discussed later. The optimized lattice constant of MOF Mn<sub>3</sub>(C<sub>6</sub>O<sub>6</sub>)<sub>2</sub> is  $a = b = 13.909$  Å, and the distance between two C atoms is about 1.465 Å, while the length of the Mn-O bond is about 2.097 Å.

Before investigating its electronic band structures, the stability of the lattice should be confirmed. We have calculated the phonon spectra for Mn<sub>3</sub>(C<sub>6</sub>O<sub>6</sub>)<sub>2</sub> monolayer, as shown in Fig. 1(c). There is no imaginary frequency throughout the Brillouin zone, indicating the excellent dynamical stability of the material. We also perform the *ab initio* molecular dynamics calculated in a 3 × 3 × 1 supercell to estimate the thermal stability for MOF Mn<sub>3</sub>(C<sub>6</sub>O<sub>6</sub>)<sub>2</sub>. As shown in Fig. 1(d), after 3000 steps at 300 K, we find that there exist thermal-induced fluctuations without bond breakage or geometric reconfigurations in the final states, demonstrating its thermal stability at room temperature. In addition, we notice that several MOF

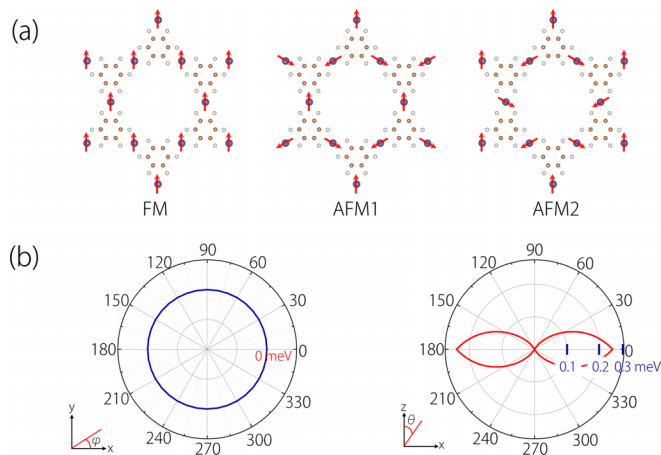


FIG. 2. (a) Possible magnetic configurations considered: ferromagnetic (FM), and possibly antiferromagnetic (AFM) structures in a  $\sqrt{3} \times \sqrt{3} \times 1$  supercell of monolayer  $\text{Mn}_3(\text{C}_6\text{O}_6)_2$ . (b) The magnetic anisotropy energy upon rotating the spin within the  $x$ - $y$  and  $z$ - $x$  planes; the blue and the red lines represent the fitted curves.

materials with the same crystal structure have already been synthesized, such as  $\text{Cu}_3(\text{C}_6\text{O}_6)_2$  [48],  $\text{Ni}_3(\text{C}_6\text{S}_6)_2$  [49], and  $\text{X}_3(\text{C}_6\text{N}_6\text{H}_6)_2$  [50,51], by various methods including a kinetically controlled approach with a competing coordination reagent, bottom-up method. Most of the above examples are nonmagnetic (or magnetic) semiconductors. Following similar methods,  $\text{Mn}_3(\text{C}_6\text{O}_6)_2$  is also promising to be synthesized in future.

The presence of transition metal ions Mn, which have partially filled  $d$  orbitals, may provide the magnetic properties required. To determine the ground magnetic configuration of  $\text{Mn}_3(\text{C}_6\text{O}_6)_2$  monolayer, we consider three possible magnetic structures including two spin frustration configurations, which are typical in kagome lattice [52]: the ferromagnetic (FM) state, and two noncollinear antiferromagnetic states (AFM1, AFM2) in a  $\sqrt{3} \times \sqrt{3} \times 1$  supercell. To determine the magnetic configuration of the MOF  $\text{Mn}_3(\text{C}_6\text{O}_6)_2$ , we considered three possible structures: the FM state, and two AFM states (AFM1, AFM2) in a  $\sqrt{3} \times \sqrt{3} \times 1$  supercell, as shown in Fig. 2(a). For the  $3d$  electrons of Mn, the effective  $U$  value is generally lower than 3.5 eV, as applied in previous works [53–55]. We have compared the energy among different magnetic configurations (FM, AFM1, and AFM2) with different  $U$  values (0–3.5 eV) under both GGA+ $U$  and LDA+ $U$  calculations. The results show that the FM configuration always has the lowest energy (see the Supplemental Material [56]), indicating the MOF  $\text{Mn}_3(\text{C}_6\text{O}_6)_2$  tends to form the FM ordering.

We have also performed Monte Carlo simulations to estimate the Curie temperature ( $T_c$ ) of  $\text{Mn}_3(\text{C}_6\text{O}_6)_2$  monolayer [57]. Our calculations show that the material has a high  $T_c$  of 171 K (see the Supplemental Material [56]), which well agrees with previous calculations [58]. Therefore, we investigated the electronic band structure of the monolayer  $\text{Mn}_3(\text{C}_6\text{O}_6)_2$  in the FM order. To determine the easy axis for the FM state, we estimated the magnetic anisotropy energy using DFT+ $U$ +SOC calculations (with  $U = 2.0$  eV) while

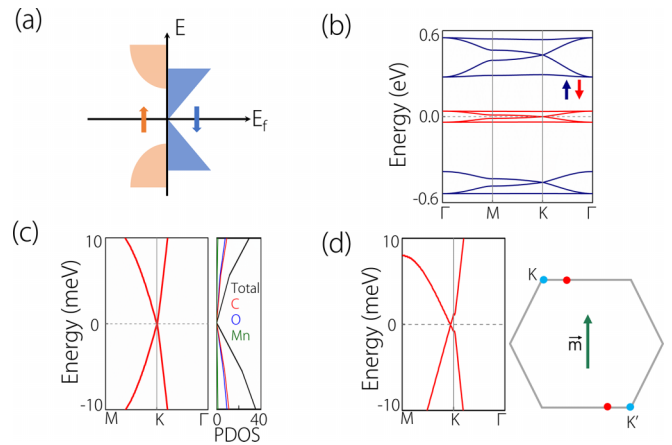


FIG. 3. (a) Schematic rule for Weyl half-semimetal. (b) Electronic band structure without spin-orbit coupling (SOC). (c) Enlarged map of energy bands near the Fermi level and corresponding projective density of states (PDOS) for the monolayer  $\text{Mn}_3(\text{C}_6\text{O}_6)_2$ . (d) The band structure with ten-times SOC. Two Weyl points are located at the  $K/K'$  points without SOC (blue points), and they are shifted along the  $x$  direction after considering SOC (red points).

rotating the spin within the  $x$ - $y$  and  $z$ - $x$  planes. As presented in Fig. 2(b), the easy magnetic axis lies in the  $x$ - $y$  plane, exhibiting an isotropic property, and the maximal value is 0.24 meV per cell lower than that of out-of-plane magnetization. Notably, the soft magnetic property of the MOF  $\text{Mn}_3(\text{C}_6\text{O}_6)_2$  indicates that its magnetization can be easily controlled by an external field.

## B. Electronic band structure

After determining the ground state for MOF  $\text{Mn}_3(\text{C}_6\text{O}_6)_2$ , we plot the electronic band structure of  $\text{Mn}_3(\text{C}_6\text{O}_6)_2$  without considering SOC in Fig. 3(b). It can be observed that spin-up and spin-down states are completely separated, and the states around the Fermi level are mainly contributed by spin-down states. In the enlarged view of the states around the  $K$  point, one can observe a 2D Weyl point, which arises solely from the spin-down state [see Fig. 3(c)], making MOF  $\text{Mn}_3(\text{C}_6\text{O}_6)_2$  a Weyl half-metal with full spin polarization.

Before considering the electronic band structure with SOC, we first determine the magnetization for the FM ground state, which was found to prefer in-plane orientation. If the magnetization direction is set perpendicular to  $M_{v1}$ , including SOC allows for the presence of this vertical mirror symmetry. This symmetry still protects the 2D Weyl points, but causes a shift in their position along the  $K$ - $M$  path. Given the weak SOC in  $\text{Mn}_3(\text{C}_6\text{O}_6)_2$ , we plot the band structure with a ten-times larger SOC in Fig. 3(d). As expected, we observe a significant shift in the position of the Weyl points.

To characterize the topological features around the Fermi level with or without SOC, we can construct an effective  $\mathbf{k} \cdot \mathbf{p}$  model around the band crossing. When SOC is not taken into account, the spin-up and spin-down states are completely decoupled, and all symmetries are preserved for each spin channel. At the  $K$  point, the point group is  $C_{3v}$ , generated by the  $C_{3z}$  rotation and a vertical mirror symmetry ( $M_{v1}$ , which is effectively a mirror symmetry along the  $y$  axis). The effective

model ( $H_K$ ) that describes the states at the  $K$  point must respect these two operations, specifically,

$$C_{3z}H_K(k)C_{3z}^{-1} = H_K(ck_x - sk_y, sk_x + ck_y), \quad (2)$$

$$M_{v1}H_K(k)M_{v1}^{-1} = H_K(k_x, -k_y), \quad (3)$$

with  $c = \cos 2\pi/3$ ,  $s = \sin 2\pi/3$ . One has checked that the crossing bands are characterized by different eigenvalues of  $C_{3z}$ , namely,  $e^{\pm i2\pi/3}$ , and taking the eigenstates of  $C_{3z}$  as the basis to construct the effective model, two independent operations can be written in the form of

$$C_{3z} = \cos \frac{2\pi}{3} \sigma_0 - i \sin \frac{2\pi}{3} \sigma_z, \quad M_{v1} = \sigma_x. \quad (4)$$

Therefore, the effective model characterizing the 2D Weyl point is given by

$$\mathcal{H}_{K/K'} = v(\pm k_x \sigma_x + k_y \sigma_y). \quad (5)$$

Here, “ $\pm$ ” corresponds to the  $K$  and  $K'$  points, respectively. The linear dispersion in the effective model is consistent with our result in DFT calculation.

When turning on SOC, the presence of magnetization strongly affects crystal symmetry. For concreteness, if setting the magnetization direction along the  $x$  axis,  $M_{v1}$  is still preserved, but threefold rotation symmetry is destroyed. In this case, a SOC term is allowed by  $M_{v1}$ , which can be expressed as  $H_{\text{SOC}} = \Delta_{\text{SOC}} \sigma_x$ . Consequently, the effective model will be

$$\mathcal{H}(K) = H_{K/K'} = v[(\pm k_x + \Delta_{\text{SOC}}/v)\sigma_x + k_y \sigma_y]. \quad (6)$$

From the effective model, we can see that when SOC is included but a vertical mirror symmetry is preserved, a 2D Weyl point is maintained, albeit with changed positions. The results described by the effective model are consistent with those derived from DFT calculations, which indicate that 2D Weyl points can be realized in MOF  $\text{Mn}_3(\text{C}_6\text{O}_6)_2$  with or without SOC. Furthermore, the presence of mirror symmetry also results in spin polarization, along the  $y$  direction. Hence,  $\text{Mn}_3(\text{C}_6\text{O}_6)_2$  is a WHS.

Because of the soft nature of this MOF material, the magnetization direction can be achieved by an external field. With an out-of-plane magnetization, the horizontal mirror symmetry  $M_z$  could be allowed. It is well known that a mirror symmetry could protect a nodal loop in the Brillouin zone. Therefore, any generic band-crossing point in the  $x$ - $y$  plane that is invariant subspace of  $M_z$ , is not isolated but belongs to a point on a nodal loop. This leads to a Weyl half-nodal loop semimetal [59].

### C. Tunable QAH phase

When the mirror symmetry  $M_{v1}$  is destroyed, the Weyl point becomes gapped. According to Eq. (7), the  $\Delta\sigma_z$  mass term can gap the Weyl point since  $\{H, \sigma_z\} = 0$ . In this case, the gapped phase can be described as

$$\mathcal{H} = v[(\pm k_x + \Delta_{\text{SOC}}/v)\sigma_x + k_y \sigma_y] + \Delta\sigma_z. \quad (7)$$

Similar to the case in graphene, the gap opening at the Weyl point induces a finite Berry curvature, which is defined as  $\Omega_z = \nabla_k \times \langle u_o | i\nabla_k | u_o \rangle$ , where  $u_o$  is the Bloch state for the

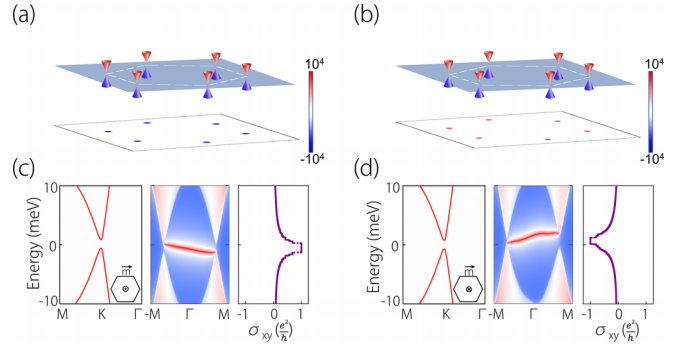


FIG. 4. (a) and (b) The distribution of the Berry curvatures for monolayer  $\text{Mn}_3(\text{C}_6\text{O}_6)_2$  with out-of-plane magnetization along  $z$  and  $-z$  direction, respectively. (c) and (d) Bulk band structure of monolayer  $\text{Mn}_3(\text{C}_6\text{O}_6)_2$  along the high-symmetry line and corresponding projective spectra, anomalous Hall conductivity in the presence of spin-orbit coupling and magnetization in the  $z$  and  $-z$  directions.

occupied band. Consequently, the Berry curvature is given by

$$\Omega_z = \pm v^2 \frac{\Delta}{2\varepsilon_o^3}. \quad (8)$$

Here,  $\varepsilon_o$  is the eigenenergy for the occupied band. This result suggests that changing the sign of the mass term also changes the sign of the Berry curvature. Additionally, the presence of this mass term breaks  $T$ , resulting in a nonzero Chern number upon integrating the Berry curvature in the Brillouin zone. Specifically, it can be derived that  $|C| = 1$ , with the sign of the Chern number determined by the sign of  $\Delta$ . The nonzero Chern number signifies a transition from a 2D Weyl phase to the QAH phase.

To demonstrate this result, we realize such a mass term by tuning the magnetization to the out-of-plane direction. In this case, the vertical mirror symmetry is broken, 2D Weyl points open an energy gap (about 1.5 meV) [as indicated in Figs. 4(c) and 4(d)], thus leading to a finite Berry curvature, as demonstrated in Figs. 4(a) and 4(b), with  $+z$  and  $-z$  magnetization, respectively. One has calculated the Chern number  $C = 1$  for these two cases. As well known, the chiral edge state is a hallmark of the QAH effect, which is evident from the presence of chiral edge states within the energy gap induced by magnetization, illustrated in Figs. 4(c) and 4(d), respectively. Furthermore, the direction of propagation of the edge states reverses with the opposite Chern number, indicating an opposite slope of the edge state. These chiral edge states contribute to a quantized Hall conductance, given by  $\sigma_{xy} = Ce^2/h$ , as demonstrated in Figs. 4(c) and 4(d). This result is in line with our theoretical analysis. Here, we want to point out that, because the bands near the Fermi level are mostly contributed by the C and O atoms, the SOC gap in  $\text{Mn}_3(\text{C}_6\text{O}_6)_2$  for the QAH state is quite small, being similar to other QAH states based on MOF materials including  $\text{CuC}_{21}\text{N}_3\text{H}_{15}$  ( $\sim 2.2$  meV) [60],  $\text{Mn}_3(\text{C}_6\text{S}_6)_2$  ( $\sim 2.4$  meV) [54], and  $\text{XC}_{21}\text{N}_3\text{H}_{15}$  ( $X = \text{Ti}, \text{Zr}, \text{Ag}, \text{Au}$ ) series ( $< 7.1$  meV) [61]. Because of the tiny SOC gaps, detection of the chiral edge modes in these MOF materials should be a challenge. However, we notice that, even though the bands are not gapped in several in-plane directions, the Berry curvature contributed by the pair of Weyl points is

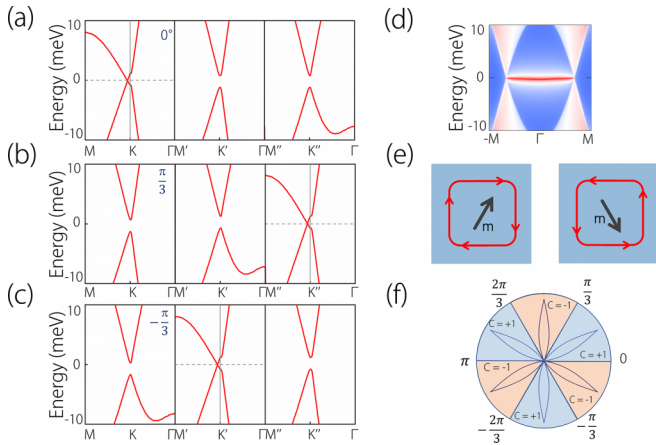


FIG. 5. [(a)–(c)] The band structures of the  $\text{Mn}_3(\text{C}_6\text{O}_6)_2$  monolayer under ten times SOC with in-plane magnetization along the  $0$ ,  $\frac{\pi}{3}$ , and  $-\frac{\pi}{3}$  axis, respectively. (d) The  $[100]$  edge state of  $\text{Mn}_3(\text{C}_6\text{O}_6)_2$ . (e) Schematic top view of a sample of finite size. The propagation direction of the chiral edge channel can be switched by tuning the magnetization direction. (f) The flowerlike curve shows the band gap as a function of the azimuthal angle  $\varphi$  of the magnetization direction. The polar radius represents the gap value. The blue (orange) areas indicate regions with a Chern number ( $C$ ) of  $+1$  ( $-1$ ).

still opposite (see the Supplemental Material [56]). Thus, the edge Fermi arc connecting a pair of Weyl points is also chiral.

Due to the isotropic property of the in-plane magnetization, its direction can be easily adjusted. In particular, there are three equal vertical mirror symmetries in the Brillouin zone; when one of them is preserved, a pair of Weyl points locating on a path parallel to the mirror symmetry can exist, but away from the  $K/K'$  points. In comparison, the other two pairs of Weyl points, protected by the remaining two mirror symmetries, are gapped, as demonstrated in Figs. 5(a)–5(c). The remaining pair of Weyl points still retains the original nature of its original ones at the  $K/K'$  points, and an edge state connects them, as demonstrated in Fig. 5(d). Notably, the gapped ones can be characterized by a nonzero Chern number. In addition, since these two gapped phases induced by breaking  $M_{v2}$  and  $M_{v3}$  are related by the mirror symmetry  $M_{v1}$  (marked by the blue and orange regions in Fig. 1(c), their Chern numbers have opposite sign, as shown in Fig. 5(f).

Then, we conclude that the Weyl point is a critical point where the Chern number inverses its sign.

To further confirm this conclusion, we plot the band gap and Chern number as the function of azimuthal angle ( $\varphi$ ) for the magnetization direction. Upon rotating its direction in plane, we find that 2D Weyl points appear when  $\varphi = 0, \pm\frac{\pi}{3}, \pm\frac{2\pi}{3}$ , or  $\pi$ , due to the preservation of one of the vertical mirror symmetries. Otherwise, the phase is the QAH phase with a nonzero Chern number, as shown in Fig. 5(f). Moreover, as the magnetization direction passes any of these five angles, the Chern number acquires a negative sign. This means that the Weyl point is indeed located at the point where the QAH phase changes its Chern number sign, which is accompanied by a switch in the propagating direction of the edge states [see Fig. 5(e)].

#### IV. CONCLUSIONS

In conclusion, we conducted a systematic investigation of the electronic and topological properties of the monolayer MOF  $\text{Mn}_3(\text{C}_6\text{O}_6)_2$  using first-principles calculations and theoretical analysis. Our results showed that the 2D time-reversal symmetry breaking Weyl point can be gapped by tuning the magnetization, driving the system to a QAH phase. Additionally, we also demonstrated that the 2D Weyl point serves as a point at the topological phase transition between two QAH phases with opposite Chern number. Indeed, in the monolayer MOF  $\text{Mn}_3(\text{C}_6\text{O}_6)_2$ , such a topological phase transition can be easily achieved due to its soft magnetic nature. Consequently, the monolayer MOF  $\text{Mn}_3(\text{C}_6\text{O}_6)_2$  offers a platform to explore the coupling between magnetism and Weyl band topology and presents an approach to design nanodevices with 2D magnetic materials.

#### ACKNOWLEDGMENTS

This work is supported by the National Natural Science Foundation of China (Grant No. 12274112) and the Natural Science Foundation of Chongqing (cstc2021jcyj-msxmX0209 and cstc2022ycjh-bgzxm0127). The work is also funded by the Overseas Scientists Sponsorship Program of Hebei Province (C20210330) and the State Key Laboratory of Reliability and Intelligence of Electrical Equipment of Hebei University of Technology (Grant No. EERI\_PI2020009).

- [1] A. A. Zyuzin and A. A. Burkov, *Phys. Rev. B* **86**, 115133 (2012).
- [2] C. Shekhar, A. K. Nayak, Y. Sun, M. Schmidt, M. Nicklas, I. Leermakers, U. Zeitler, Y. Skourski, J. Wosnitza, Z. Liu *et al.*, *Nat. Phys.* **11**, 645 (2015).
- [3] B. Yan and C. Felser, *Annu. Rev. Condens. Matter Phys.* **8**, 337 (2017).
- [4] B. Q. Lv, H. M. Weng, B. B. Fu, X. P. Wang, H. Miao, J. Ma, P. Richard, X. C. Huang, L. X. Zhao, G. F. Chen, Z. Fang, X. Dai, T. Qian, and H. Ding, *Phys. Rev. X* **5**, 031013 (2015).
- [5] D. Liu, A. Liang, E. Liu, Q. Xu, Y. Li, C. Chen, D. Pei, W. Shi, S. Mo, P. Dudin *et al.*, *Science* **365**, 1282 (2019).
- [6] W. Meng, Y. Liu, W.-W. Yu, X. Zhang, and G. Liu, *Mater. Today Phys.* **27**, 100774 (2022).
- [7] I. T. Grodsky and R. F. Streater, *Phys. Rev. Lett.* **20**, 695 (1968).
- [8] X. Wan, A. M. Turner, A. Vishwanath, and S. Y. Savrasov, *Phys. Rev. B* **83**, 205101 (2011).
- [9] T. Liang, Q. Gibson, M. N. Ali, M. Liu, R. Cava, and N. Ong, *Nat. Mater.* **14**, 280 (2015).
- [10] X. Huang, L. Zhao, Y. Long, P. Wang, D. Chen, Z. Yang, H. Liang, M. Xue, H. Weng, Z. Fang, X. Dai, and G. Chen, *Phys. Rev. X* **5**, 031023 (2015).
- [11] F. Arnold, C. Shekhar, S.-C. Wu, Y. Sun, R. D. Dos Reis, N. Kumar, M. Naumann, M. O. Ajeesh, M. Schmidt, A. G. Grushin *et al.*, *Nat. Commun.* **7**, 11615 (2016).

- [12] A. Lucas, R. A. Davison, and S. Sachdev, *Proc. Natl. Acad. Sci. USA* **113**, 9463 (2016).
- [13] C.-Z. Li, L.-X. Wang, H. Liu, J. Wang, Z.-M. Liao, and D.-P. Yu, *Nat. Commun.* **6**, 10137 (2015).
- [14] A. V. Andreev and B. Z. Spivak, *Phys. Rev. Lett.* **120**, 026601 (2018).
- [15] G. B. Osterhoudt, L. K. Diebel, M. J. Gray, X. Yang, J. Stanco, X. Huang, B. Shen, N. Ni, P. J. Moll, Y. Ran *et al.*, *Nat. Mater.* **18**, 471 (2019).
- [16] X. Zhang, W. Meng, Y. Liu, X. Dai, G. Liu, and L. Kou, *J. Am. Chem. Soc.* **145**, 5523 (2023).
- [17] W. Meng, X. Zhang, Y. Liu, X. Dai, G. Liu, Y. Gu, E. Kenny, and L. Kou, *Adv. Sci.* **10**, 2205940 (2023).
- [18] W. Meng, X. Zhang, Y. Liu, X. Dai, and G. Liu, *Phys. Rev. B* **104**, 195145 (2021).
- [19] W. Liu, X. Zhang, W. Meng, Y. Liu, X. Dai, and G. Liu, *iScience* **25**, 103543 (2022).
- [20] Z. He, W. Meng, Y. Liu, X. Zhang, and G. Liu, *J. Mater. Chem. A* **10**, 12510 (2022).
- [21] S. A. Yang, *Spin* (World Scientific, Singapore, 2016), Vol. 6, p. 1640003.
- [22] N. P. Armitage, E. J. Mele, and A. Vishwanath, *Rev. Mod. Phys.* **90**, 015001 (2018).
- [23] W.-W. Yu, Y. Liu, W. Meng, H. Liu, J. Gao, X. Zhang, and G. Liu, *Phys. Rev. B* **105**, 035429 (2022).
- [24] K. v. Klitzing, G. Dorda, and M. Pepper, *Phys. Rev. Lett.* **45**, 494 (1980).
- [25] F. D. M. Haldane, *Phys. Rev. Lett.* **61**, 2015 (1988).
- [26] C.-Z. Chang, J. Zhang, X. Feng, J. Shen, Z. Zhang, M. Guo, K. Li, Y. Ou, P. Wei, L.-L. Wang *et al.*, *Science* **340**, 167 (2013).
- [27] J. Checkelsky, R. Yoshimi, A. Tsukazaki, K. Takahashi, Y. Kozuka, J. Falson, M. Kawasaki, and Y. Tokura, *Nat. Phys.* **10**, 731 (2014).
- [28] X. Kou, S.-T. Guo, Y. Fan, L. Pan, M. Lang, Y. Jiang, Q. Shao, T. Nie, K. Murata, J. Tang, Y. Wang, L. He, T.-K. Lee, W.-L. Lee, and K. L. Wang, *Phys. Rev. Lett.* **113**, 137201 (2014).
- [29] A. J. Bestwick, E. J. Fox, X. Kou, L. Pan, K. L. Wang, and D. Goldhaber-Gordon, *Phys. Rev. Lett.* **114**, 187201 (2015).
- [30] T. He, X. Zhang, L. Wang, Y. Liu, X. Dai, L. Wang, and G. Liu, *Mater. Today Phys.* **17**, 100360 (2021).
- [31] J.-Y. You, C. Chen, Z. Zhang, X.-L. Sheng, S. A. Yang, and G. Su, *Phys. Rev. B* **100**, 064408 (2019).
- [32] L. Jin, L. Wang, X. Zhang, Y. Liu, X. Dai, H. Gao, and G. Liu, *Nanoscale* **13**, 5901 (2021).
- [33] J. Lee, O. K. Farha, J. Roberts, K. A. Scheidt, S. T. Nguyen, and J. T. Hupp, *Chem. Soc. Rev.* **38**, 1450 (2009).
- [34] J. L. Rowsell and O. M. Yaghi, *Microporous Mesoporous Mater.* **73**, 3 (2004).
- [35] H.-C. Zhou, J. R. Long, and O. M. Yaghi, *Chem. Rev.* **112**, 673 (2012).
- [36] X. Zhang, A. Wang, and M. Zhao, *Carbon* **84**, 1 (2015).
- [37] A. Wang, X. Zhang, Y. Feng, and M. Zhao, *J. Phys. Chem. Lett.* **8**, 3770 (2017).
- [38] F. Lv, F. Feng, F. Shang, Q. Chuai, and G. Wang, *Acta Phys. Pol., A* **137**, 1158 (2020).
- [39] G. Kresse and J. Furthmüller, *Phys. Rev. B* **54**, 11169 (1996).
- [40] G. Kresse and J. Furthmüller, *Comput. Mater. Sci.* **6**, 15 (1996).
- [41] D. M. Ceperley and B. J. Alder, *Phys. Rev. Lett.* **45**, 566 (1980).
- [42] J. P. Perdew, K. Burke, and M. Ernzerhof, *Phys. Rev. Lett.* **77**, 3865 (1996).
- [43] H. J. Monkhorst and J. D. Pack, *Phys. Rev. B* **13**, 5188 (1976).
- [44] K. Momma and F. Izumi, *J. Appl. Crystallogr.* **44**, 1272 (2011).
- [45] N. Marzari and D. Vanderbilt, *Phys. Rev. B* **56**, 12847 (1997).
- [46] A. A. Mostofi, J. R. Yates, Y.-S. Lee, I. Souza, D. Vanderbilt, and N. Marzari, *Comput. Phys. Commun.* **178**, 685 (2008).
- [47] Q. Wu, S. Zhang, H.-F. Song, M. Troyer, and A. A. Soluyanov, *Comput. Phys. Commun.* **224**, 405 (2018).
- [48] J. Park, A. C. Hinckley, Z. Huang, D. Feng, A. A. Yakovenko, M. Lee, S. Chen, X. Zou, and Z. Bao, *J. Am. Chem. Soc.* **140**, 14533 (2018).
- [49] T. Kambe, R. Sakamoto, K. Hoshiko, K. Takada, M. Miyachi, J.-H. Ryu, S. Sasaki, J. Kim, K. Nakazato, M. Takata *et al.*, *J. Am. Chem. Soc.* **135**, 2462 (2013).
- [50] J. Park, M. Lee, D. Feng, Z. Huang, A. C. Hinckley, A. Yakovenko, X. Zou, Y. Cui, and Z. Bao, *J. Am. Chem. Soc.* **140**, 10315 (2018).
- [51] D. Feng, T. Lei, M. R. Lukatskaya, J. Park, Z. Huang, M. Lee, L. Shaw, S. Chen, A. A. Yakovenko, A. Kulkarni *et al.*, *Nat. Energy* **3**, 30 (2018).
- [52] D. Grohol, K. Matan, J.-H. Cho, S.-H. Lee, J. W. Lynn, D. G. Nocera, and Y. S. Lee, *Nat. Mater.* **4**, 323 (2005).
- [53] J. Zhou and Q. Sun, *J. Am. Chem. Soc.* **133**, 15113 (2011).
- [54] M. Zhao, A. Wang, and X. Zhang, *Nanoscale* **5**, 10404 (2013).
- [55] Y. Wang, W. Ji, C. Zhang, P. Li, P. Wang, B. Kong, S. Li, S. Yan, and K. Liang, *Appl. Phys. Lett.* **110**, 233107 (2017).
- [56] See Supplemental Material at <http://link.aps.org/supplemental/10.1103/PhysRevB.108.054404> for different calculation methods and magnetic configurations on magnetic properties of  $\text{Mn}_3(\text{C}_6\text{O}_6)_2$ , and the topological properties of  $\text{Mn}_3(\text{C}_6\text{O}_6)_2$ .
- [57] L. Liu, X. Ren, J. Xie, B. Cheng, W. Liu, T. An, H. Qin, and J. Hu, *Appl. Surf. Sci.* **480**, 300 (2019).
- [58] S. Kang and J. Yu, *Phys. Chem. Chem. Phys.* **24**, 22168 (2022).
- [59] R.-W. Zhang, X. Zhou, Z. Zhang, D.-S. Ma, Z.-M. Yu, W. Feng, and Y. Yao, *Nano Lett.* **21**, 8749 (2021).
- [60] J. Zhang, B. Zhao, C. Ma, and Z. Yang, *Appl. Phys. Lett.* **114**, 043102 (2019).
- [61] C.-Q. Chen, X.-S. Ni, D.-X. Yao, and Y. Hou, *Appl. Phys. Lett.* **121**, 142401 (2022).